




## Phase diagram of brittle fracture in the semi-grand-canonical ensemble

T. Mulla,<sup>1</sup> S. Moeini ,<sup>1</sup> K. Ioannidou,<sup>1,2,3</sup> R. J.-M. Pellenq ,<sup>1,2,4</sup> and F.-J. Ulm ,<sup>1,2,\*</sup>

<sup>1</sup>Department of Civil and Environmental Engineering, Massachusetts Institute of Technology, Cambridge, Massachusetts 02139, USA

<sup>2</sup>MIT-CNRS-AMU Joint Laboratory, Massachusetts Institute of Technology, Cambridge, Massachusetts 02139, USA

<sup>3</sup>Laboratoire de Mécanique et Génie Civil, CNRS Université de Montpellier, 34090 Montpellier, France

<sup>4</sup>Department of Physics, Georgetown University, Washington DC 20057, USA



(Received 1 June 2020; revised 2 October 2020; accepted 21 December 2020; published 13 January 2021)

We present a simulation method to assess the quasistatic fracture resistance of materials. Set within a semi-grand-canonical Monte Carlo (SGCMC) simulation environment, an auxiliary field—the bond rupture potential—is introduced to generate a sufficiently large number of possible microstates in the semi-grand-canonical ensemble, and associated energy and bond fluctuations. The SGCMC approach permits identifying the full phase diagram of brittle fracture for harmonic and nonharmonic bond potentials, analogous to the gas-liquid phase diagram, with the equivalent of a liquidus line ending in a critical point. The phase diagram delineates a solid phase, a fractured phase, and a gas phase, and provides clear evidence of a first-order phase transition intrinsic to fracture. Moreover, energy and bond fluctuations generated with the SGCMC approach permit determination of the maximum energy dissipation associated with bond rupture, and hence of the fracture resistance of a widespread range of materials that can be described by bond potentials.

DOI: [10.1103/PhysRevE.103.013003](https://doi.org/10.1103/PhysRevE.103.013003)

### I. INTRODUCTION

Consider a solid composed of particles subjected to a volume change at constant temperature. The system is further subjected to an external energy source that targets the bonds in the system, akin to a bulk radiation source. At a given energy of this radiation source, denoted by  $\Delta\mu$ , fracture at the macroscopic level of the sample may occur between two equilibrium states of the system. This transition is defined by the bond rupture potential,  $\Delta\mu$ , the prescribed volume,  $V$ , and temperature,  $T$ . In this semi-grand-canonical ensemble, we measure the ensemble energy average of possible microstates of the system,  $\langle U \rangle$ , and the energy fluctuations, as a function of the average number of bonds,  $\langle N \rangle$ , and their fluctuations. As we repeat the experiment by sweeping possible values for volume changes, stress-strain curves can be traced out for different prescribed bond potentials,  $\Delta\mu$  [Figs. 1(a) and 1(b)]. Similarly, sweeping all possible values of  $\Delta\mu$  we obtain characteristic bond isochores,  $\langle N \rangle - \Delta\mu$ , for different prescribed volume strains [Figs. 1(c) and 1(d)].

The described thought experiment aims at addressing some unsolved issues in fracture mechanics, such as homogenization of fracture properties of heterogeneous solids, which cannot be satisfactorily resolved with classical continuum theories based on Griffith's 1921 energy-based quasistatic fracture approach [1,2], that requires notches and other discontinuities to trigger fracture propagation, local stress intensities [3], and cohesive crack zones [4–7] to determine the fracture resistance of solids. More contemporary simulation approaches have extended the realm of classical fracture mechanics to discrete (including molecular) fracture processes [8–10]. Statistical lattice-based models of fracture

addressed size effects of materials' strength, bursts of microfailures, and morphology of cracks [9–13]. Others consider the competition between crack propagation and dislocation mechanisms [14–16]; role of interatomic and mean force potentials [17–21]; role of phonons [18,22,23]; crack velocity and dynamic instability [20,24–27]; crack growth kinetics of microcracks in crystals [28]; and effect of crystal orientation, grain boundaries, texture, chemical environment, and impurities [25,29–35]. Compared to this rich and insistently increasing body of fracture literature, our approach differs in two fundamental aspects: (1) it defines the fracture process as bond rupture in the semi-grand-canonical ensemble ( $\Delta\mu VT$ ), in contrast to the canonical ( $NVT$ ) and microcanonical ( $NVE$ ) ensembles that restrain our current knowledge of the physics of fracture processes; and by doing so (2) it enables a new understanding of fracture resistance of solids, in terms of energy and bond fluctuations, in the  $\Delta\mu VT$  ensemble.

We start by rationalizing the thought-experiment into a simulation framework for equilibrium-based fracture analysis. First, we perform the thought-experiment by means of almost classical Monte Carlo simulations [36], with one exception: instead of inserting or deleting randomly selected particles (GCMC), the acceptance criterion in the SGCMC approach changes the identity of bonds:

$$\text{acc}(o \rightarrow n) = \min(1, p_{o \rightarrow n}), \quad (1)$$

where  $p_{o \rightarrow n}$  stands for the probability of either switching a bond from OFF to ON, ( $N \rightarrow N + 1$ ), or from ON to OFF ( $N \rightarrow N - 1$ ):

$$p_{N \rightarrow N+1} = \exp\left[\frac{1}{k_B T} (+\Delta\mu - \Delta U_{N \rightarrow N+1})\right], \quad (2a)$$

$$p_{N \rightarrow N-1} = \exp\left[\frac{1}{k_B T} (-\Delta\mu - \Delta U_{N \rightarrow N-1})\right], \quad (2b)$$

\*Corresponding author: [ulm@mit.edu](mailto:ulm@mit.edu)

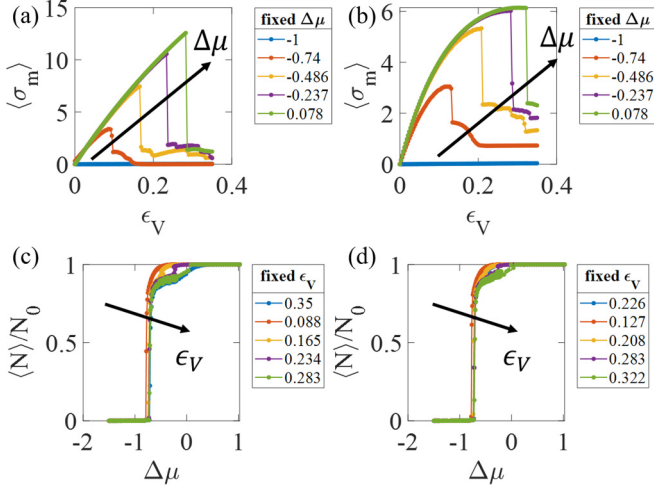


FIG. 1. Work-conjugate pairs in the semi-grand-canonical ensemble. At fixed bond potential  $\Delta\mu$ , successive MC simulations at different prescribed strains trace out a stress-strain curve for (a) harmonic and (b) Morse potentials. For a fixed volume strain, at different  $\Delta\mu$ , bond number  $N$  is measured generating bond isochores for (c) harmonic and (d) Morse potentials.

with  $\Delta U_{o \rightarrow n} = U_n - U_o$  the difference in potential energy of microstate  $\mathcal{M} = (o, n)$ .

## II. PHASE DIAGRAM OF BRITTLE FRACTURE

We now corroborate the predictive power of the proposed SGCMC bond-fracture approach. For illustration, we consider a  $10 \times 10 \times 10$  face-centered cubic (FCC) lattice with four atoms in each unit cell (4000 atoms in total,  $N_0 = 24\,000$  bonds), and periodic boundary conditions. Simulations start with fully bonded particles. Two types of bond potentials are considered: a truncated harmonic potential and the Morse potential [37]. We begin with an analysis of recorded stress-strain curves [Figs. 1(a) and 1(b)]. In the semi-grand-canonical ensemble, we prescribe the volume in the form  $V = V_0(1 + \epsilon_V)$ , where  $V_0$  is the volume of the undeformed simulation box, and  $\epsilon_V$  the volume strain. In this displacement-controlled test setup, simulations are carried out at different volume strains, whereas the bond potential,  $\Delta\mu$ , is held constant over the entire range of the volume strain applied. The displacement-controlled test setup is repeated for different values of  $\Delta\mu$ . The impact of the prescribed bond potential on the stress-strain response is shown in Figs. 1(a) and 1(b), in the form of a decrease in stress-strain capacity with decreasing bond potential. Alternatively, in a bond potential-controlled setup, we analyze the work-conjugated bond number  $N$  at constant volume strain, i.e., the bond isochores [Figs. 1(c) and 1(d)]. Akin to a gas, the number of bonds goes to zero as the bond potential tends to negative values, whereas no bonds break when bond potential tends to positive values. The bond isochores [Figs. 1(c) and 1(d)] provide a means to understand the flattening of the stress-strain response [Figs. 1(a) and 1(b)] with decreasing bond potential. Indeed, the lowering of the bond potential entails bond breakage, which ultimately shifts the system from a bonded solid state to an unbonded gaslike state.

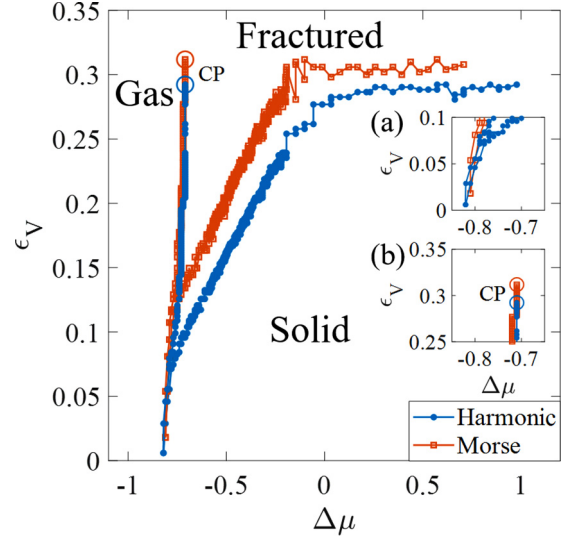


FIG. 2. Phase diagrams of brittle fracture for harmonic (closed circles) and Morse (open squares) bond potential systems. The phase diagram is characterized by three domains corresponding to (I)  $\Delta\mu < \Delta\mu_{\text{gas}}$ : the system is a collection of non-interacting particles and cannot undergo fracture. The line terminates in a critical point, CP (near-vertical line,  $\Delta\mu$  controlled). (II)  $\Delta\mu_{\text{gas}} \leq \Delta\mu \leq 0$ : solid undergoes fracture when  $\epsilon_V > \epsilon_{V_{\text{crit}}}$  or  $\Delta\mu < \Delta\mu_{\text{crit}}$  (sloped line). (III)  $\Delta\mu > 0$ : fracture is controlled by constant  $\epsilon_{V_{\text{crit}}}$  (flat line). Insets: (a) Near zero strain the phase boundaries meet at a triple point. (b) Liquidus lines terminate at a CP.

The analysis of the stress-strain diagrams and bond isochores calls for a generalization in form of a phase diagram. This is achieved by sweeping the  $(\Delta\mu, V)$  phase space in search of phase boundaries defined by the pair of coordinates at which fracture occurs, namely the critical bond rupture potential [ $\Delta\mu_{\text{crit}} = \Delta\hat{\mu}_{\text{crit}}(\langle N \rangle_{\text{crit}})$ ] and the critical volumetric strain [ $V_{\text{crit}} = V_0(1 + \epsilon_{V_{\text{crit}}})$ ]. Figure 2 displays the phase diagrams for the harmonic and Morse potentials, including the transition lines between solid and gas state of the system. Irrespective of the bond potential, the phase boundary begins with a near vertical line delineating the minimum bond rupture potential below which the system is effectively a gas (domain I), and above which the bonded system is fractured or a solid. In this domain, the phase diagram has much in common with classical pressure-temperature phase diagrams of pure substances, when considering the prescribed strain as the analog of temperature, the prescribed bond rupture potential as the analog of pressure, and the fractured state as the analog of the liquid phase. In fact, the phase line starts at a triple point close to  $\epsilon_V = 0$  [inset (a) in Fig. 2], and terminates in a critical point, CP [inset (b) in Fig. 2]. In between these two, we recognize—by analogy with pressure-temperature phase diagrams—the existence of a liquidus line, along which the bond rupture potential has such a low value that bonds dissolve (rather than fracture due to bond stretching) independently of the applied strain. The system is thus reduced to a collection of noninteracting particles. In this unbonded ( $N = 0$ ) gaslike state there are effectively no interactions. Mapped onto the pressure-temperature analogy, the measured critical exponents near the critical point where the liquidus

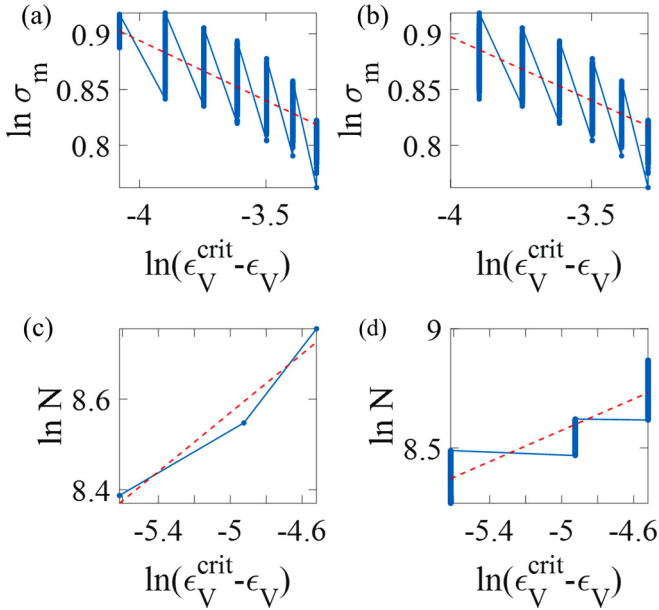


FIG. 3. Critical exponents fit from the simulation results. Lower and upper bounds of the fits (red dashed lines) for the stress critical exponent,  $\alpha$  [(a) and (b), respectively], as well as for the bond number critical exponent,  $\beta$  [(c) and (d), respectively] are in good agreement with the same exponents in the Ising model.

line ends fall in the range of  $0.1075 < \alpha < 0.114$ , when extending the analogy to include the mean stress as the analog of the isochoric heat capacity in the Ising model. Similarly, taking the bond number as the analog of the magnetic order parameter, we can measure  $0.3246 < \beta < 0.3292$  (see Fig. 3), in close agreement with the values of the three-dimensional Ising model ( $\alpha = 0.1096$  and  $\beta = 0.32653$  [38]). This shows that the proposed SGCMC model around the critical point exhibits features similar to the compressible Ising model [39], which merits further exploration.

The remaining part of the  $(\Delta\mu, \epsilon_V)$  phase diagram defines the phase transition between the solid and fractured phases. The solid-fracture phase transition is a first-order phase transition, as all work-conjugated energy derivatives (i.e., mean stress, bond number) exhibit discontinuities at fracture. Specifically, these quantities exhibit jump discontinuities at a critical value corresponding to the crossing of the phase boundary, shown for  $\Delta\mu_{crit} = 0.033$  and  $\epsilon_V^{crit} = 0.3216$  in Fig. 4. Moreover, these discontinuities occur in the first-order derivative of the energy; namely: the mean stress,  $\sigma_m = \partial U / \partial \epsilon_V$ , bond number,  $N = -\partial U (= -k_B T \ln \Xi_S) / \partial \mu$ , and heat of bond rupture,  $q_{br} = -\partial U / \partial N$ , where  $\Xi_S$  is the semi-grand-canonical partition function. The combination of these observations unambiguously defines fracture at the crossing of the phase boundary as a first-order phase transition.

Furthermore, the phase boundaries exhibit a characteristic shape, namely a phase line with a finite slope for  $\Delta\mu_{gas} < \Delta\mu < 0$  (domain II) and a horizontal line defined by a constant maximum critical strain for  $\Delta\mu > 0$  (domain III). In domain II, the solid region is characterized by strains below the phase boundary,  $\epsilon_V < \epsilon_V^{crit}$ , corresponding to stress-strain curves with a positive slope [Figs. 1(a) and 1(b)] and by bond

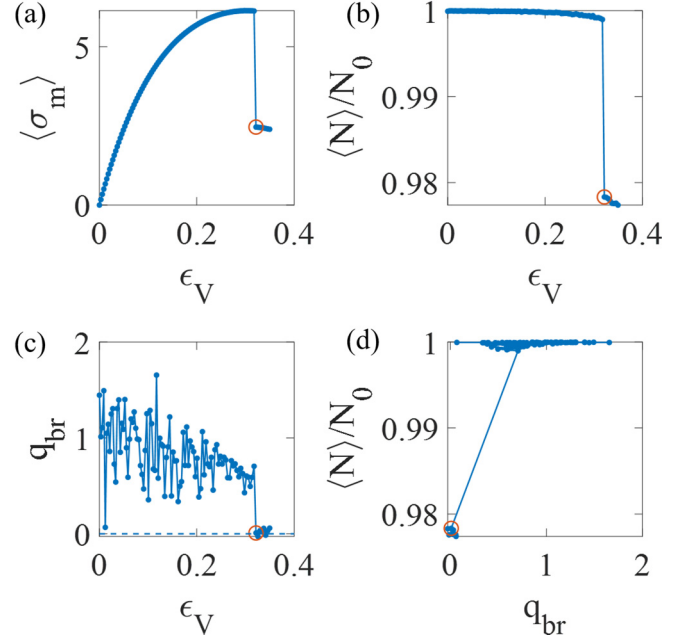


FIG. 4. First-order phase transition of brittle fracture: Jump discontinuities in (a) stress, [(b),(d)] bond number, and (c) heat of bond rupture occur at the same point (red open circles)  $q_{br} = 0$  as predicted by the fluctuation-dissipation approach to fracture mechanics.

rupture potentials to the right of the phase boundary,  $\Delta\mu > \Delta\mu_{crit}$ , in accordance with the bond isochores [Figs. 1(c) and 1(d)]. In contrast, domain III ( $\Delta\mu > 0$ ) is characterized by a maximum critical stress and strain at fracture. Increasing the bond rupture potential does not yield higher strains at fracture. These observations explain the (close to) zero slope of the phase boundary in the  $(\Delta\mu, \epsilon_V)$  space. If we remind ourselves that classical fracture mechanics operates at  $\Delta\mu = 0$  with notches or other initial discontinuities to trigger fracture propagation, we recognize from analyzing the phase diagram that  $\Delta\mu = 0$  defines the onset of the maximum critical strain holds for higher positive values of bond rupture potential as well (Fig. 2). This suggests that the constant critical strain delineating the solid-fracture phase transition is an order parameter.

To further characterize the different phases of the system, Fig. 5 displays the radial distribution functions (RDFs) obtained from simulations, together with characteristic sample snapshots of the particle energies. The RDFs illustrate the impact of fracture on relative position of the particles in consequence of the energy release due to bond breakage. In fact, as the system is strained from the undeformed reference configuration [Fig. 5(a)] to just before fracture [25.2% strain,  $\Delta\mu = -0.354$ , Fig. 5(b)] the RDF shifts to higher distance values as energy is stored into the stretched bonds. After fracture [25.6% strain, Fig. 5(c)], a part of this energy is released in bond breakage across a crack surface which leads to a visible shift of the RDF to the left (see Supplemental Material [40]). Finally, for domain I we obtain an RDF [shown for  $\Delta\mu = -1$ , Fig. 5(d)] reminiscent of an ideal gas of noninteracting particles, with a first shell distance peak much smaller

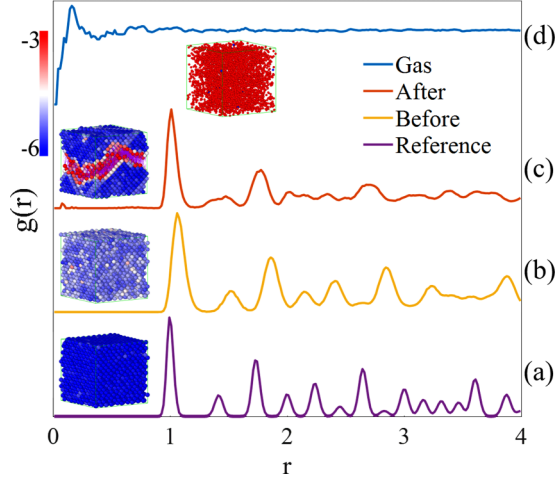


FIG. 5. Radial distribution functions around fracture and in the gas phase. Starting from (a) the reference (unstrained) state, the system is (b) stretched, storing energy and shifting the RDF peaks to higher lattice distances. Comparing the RDFs before and after fracture, (c) peaks are noticeably shifted back to lower distances, indicative of a fracture-induced energy release in the system. (d) The gas RDF approaches ideal gas behavior as the system is a set of noninteracting particles. Insets: color-coded simulation snapshots of the potential energy (color bar on the far left).

than the reference FCC lattice distance. The movie in the Supplemental Material [40] also demonstrates how damage is sustained in the system prior to catastrophic failure through a series of microcracks that form randomly throughout the material. Precursory to the macrocrack formation, several microcracks are created throughout the entire system. At a critical strain, the fluctuating number of microcracks exhibits collective behavior marked by percolation across the entire sample to form the macrocrack. This microcrack formation is heterogeneous even in the case of a homogeneous reference lattice.

### III. HEATS OF BOND RUPTURE

The last focus of our analysis is to quantitatively pin down the fracture resistance of the material. This is achieved by considering (1) the bond number fluctuations,  $\text{Var}(N) = \langle N^2 \rangle - \langle N \rangle^2$ , and (2) the associated energy fluctuations,  $\text{Cov}(U, N) = \langle UN \rangle - \langle U \rangle \langle N \rangle$ . These fluctuations, outputs from the SGCMC simulations, are key to assessing the fracture resistance of a material. In fact, akin to adsorption processes [41,42], equate energy fluctuations with the heat of bond rupture [43]:

$$q_{br} = -\frac{\partial \langle U \rangle}{\partial \langle N \rangle} = -\frac{\text{Cov}(U, N)}{\text{Var}(N)}. \quad (3)$$

Then, split the total energy  $U$  in two parts, one related to the ground-state energy of the system,  $U^0 = \sum_i^N U^i(\vec{r}_i)$ , representative of the internal bond energy (cohesion) in the absence of any deformation of the system, the other related to the deformation in consequence of, e.g., two-body interactions between particles  $i, j$ ,  $U^\lambda = \sum_{i,j}^N U^{ij}(\vec{r}_{ij} = \vec{r}_j - \vec{r}_i)$ . Consequently, a critical value of the bond rupture resistance

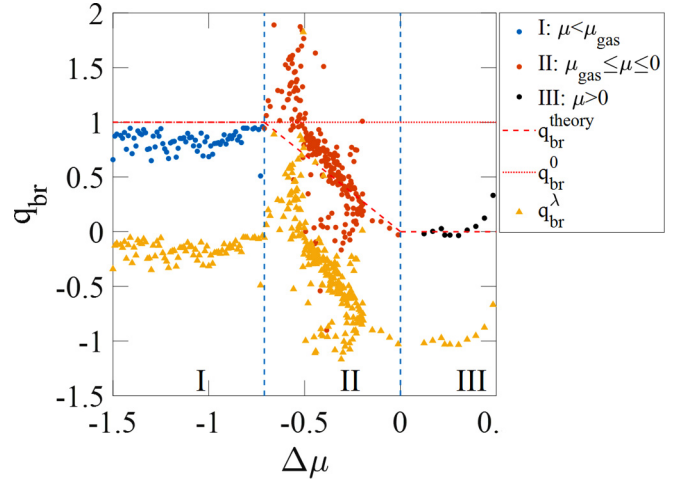


FIG. 6. Heat of bond rupture when crossing phase boundaries. There is no unique condition for fracture across all values of imposed bond rupture potential, across all domains. This is evidenced by the value of the heat of bond rupture when crossing a phase boundary in the different domains I, II, and III. Instead the value of  $q_{br}$  when crossing a phase boundary serves to identify the different domains or phases of brittle fracture across all possible values of bond rupture potential.

can be defined at which the heat associated with the change in strain energy, ( $q_{br}^\lambda = -\partial \langle U^\lambda \rangle / \partial \langle N \rangle$ ), is equal with opposite sign to the heat release due to ground-state energy release, ( $q_{br}^0 = -\partial \langle U^0 \rangle / \partial \langle N \rangle$ ); that is, for  $q_{br} = 0$ ,

$$q_{br}^\lambda = -\frac{\text{Cov}(U^\lambda, N)}{\text{Var}(N)} \equiv -q_{br}^0 = \frac{\text{Cov}(U^0, N)}{\text{Var}(N)}. \quad (4)$$

Expression (4) is nothing but Griffith's quasistatic fracture criterion [1] expressed in terms of energy fluctuations:  $-q_{br}^\lambda$  is the bond energy release rate (analogous to Griffith's energy release rate [2]), and  $q_{br}^0$  its critical value (analogous to Griffith's fracture energy). In this sense, for  $-q_{br}^\lambda < q_{br}^0$ , there are still enough strain energy reserves in the system to redistribute the elastic strain energy due to a prescribed volume change without further bond breakage. This process can be associated with a stable bond fracture process. In contrast, for  $-q_{br}^\lambda > q_{br}^0$ , the system has exhausted its maximum energy release capacity, defined by Eq. (4), releasing more ground-state energy in the form of heat than redistributing work internally in form of recoverable energy. This is shown in Fig. 6 for the three domains identified from the phase diagram. It is of interest to condense these results into simplified bond fracture criteria. To this end, consider the probability of switching a bond ON,  $p_{N \rightarrow N+1}$ , equal to the probability of switching a bond OFF,  $p_{N \rightarrow N-1}$ , and rewrite the acceptance criteria (2), while approximating the change in energy by  $\Delta U_{N \rightarrow N+1} \simeq \partial \langle U \rangle / \partial \langle N + 1 \rangle = -q_{br}$ :

$$\exp[\beta(\Delta\mu + q_{br})] = \exp[\beta(-\Delta\mu - q_{br})], \quad (5a)$$

$$\Delta\mu = -q_{br} = -q_{br}^0 - q_{br}^\lambda. \quad (5b)$$

Equations (5) suggest two limit states that link the external fields ( $\Delta\mu, V, T$ ) to the fracture resistance  $q_{br}^0$ ; i.e.,  $0 \leq -q_{br}^\lambda = q_{br}^0 + \Delta\mu \leq q_{br}^0$  (noting that  $-q_{br}^\lambda > 0$ ).

Furthermore, the bond rupture potential exhibits two bounds,  $-q_{br}^0 \leq \Delta\mu \leq 0$ . The upper bound of Eq. (5b),  $\Delta\mu = 0$ , coincides with definition (4) of the critical bond energy release rate, and is thus recognized as the critical fracture point, associated with the maximum release of strain energy due to the dissipation of groundstate energy. The bound of  $\Delta\mu = 0$  also marks the point of equilibrium of the bond rupture potentials where  $\Delta\mu = \mu_{\text{OFF}} - \mu_{\text{ON}} = 0$ . The lower bound  $\Delta\mu = -q_{br}^0$  can be attributed to the depletion of the energy storage of the bonds before any strain is applied in accordance with Eqs. (2) and (5a). Such a drastic shift in energy content of the bonds pushes the system into a gaslike state where the most favorable configuration of the system has no bonds,  $N = 0$ . The actual lower bound found from simulations, while close to  $-q_{br}^0$ , is denoted by  $\Delta\mu_{\text{gas}}$  in order to reflect its deviation from the predicted value and to associate it with the gas phase of the system for  $\Delta\mu < \Delta\mu_{\text{gas}}$ . In between these two limit states the effect of the bond rupture potential on the potential energy of the system is absorbed by  $q_{br}^\lambda$  in the acceptance probabilities of the SGCMC moves, and therefore is visible from the bond number of the system. These limit states are summarized by the following set of fracture criteria in function of the bond rupture potential across the considered domains I, II, and III:

$$q_{br} = q_{br}^0 \begin{cases} 1, & \Delta\mu < \Delta\mu_{\text{gas}} & \text{(I)}, \\ \frac{\Delta\mu}{\Delta\mu_{\text{gas}}}, & \Delta\mu_{\text{gas}} \leq \Delta\mu \leq 0 & \text{(II)}, \\ 0, & \Delta\mu > 0 & \text{(III)}. \end{cases} \quad (6)$$

The agreement of the fracture criteria (6) with simulation results for the entire phase space is shown in Fig. 6. Specifically, domain I corresponding to the gas phase exhibits no fracture, since the system has no bonds to carry load. This results in a zero heat of stretching ( $q_{br}^\lambda = 0$ , thus  $q_{br} = q_{br}^0$ ). Domain II is characterized by a solid phase where fracture occurs before complete exhaustion of the ground-state energy of the material along fracture surfaces; hence  $q_{br} > 0$ . Finally, domain III corresponds to the solid phase where fracture occurs when the heat associated with the change in strain energy is equal with opposite sign to the heat due to ground-state energy release in accordance with Eq. (4).

#### IV. CONCLUSIONS

In summary, we have shown that quasistatic fracture mechanics in the semi-grand-canonical ensemble provides a versatile means to determine phase diagrams of brittle fracture of solids. Modularity of the framework with respect to choice of energy potential and geometry leaves open avenues for investigation of fracture of heterogeneous materials. While heats of bond rupture in the context of fracture have not been measured, the simulation measurements can still be compared to existing fracture resistance measurement techniques. Furthermore, heats of bond rupture formulated in this work can—at least theoretically—be measured through calorimetry experiments. This work can lead to better understanding and implementation of such experiments in the future. Furthermore, the approach permits assessment of the fracture resistance of materials based upon fluctuations without the need to concentrate these fluctuations into notches and other discontinuities. The fact that the proposed semi-grand-canonical method is not limited by bond potential expressions

and geometric texture of materials provides a promising venue to investigate fracture phenomena of heterogeneous materials with reference to the intimate interplay between structure and fracture resistance.

#### ACKNOWLEDGMENTS

This research was carried out by the Concrete Sustainability Hub at MIT, with funding provided by the Portland Cement Association (PCA, Skokie IL, US) and the Ready Mixed Concrete Research & Education Foundation (Maryland, US). We are grateful for discussions with and advice of Prof. Mehran Kardar at MIT.

#### APPENDIX: METHODS

Simulations are carried out in the semi-grand-canonical (SGC) ensemble. The semi-grand-canonical ensemble is characterized by four prescribed state variables: total number of bonds,  $N_0$ , bond rupture potential,  $\Delta\mu$ , volume,  $V$ , and temperature,  $T$ . In contrast to the grand canonical ( $\mu VT$ ) ensemble, the SGC ensemble is termed a  $\Delta\mu VT$  ensemble, because the total numbers of bonds,  $N_0$ , is constant, admitting only a change in identity of the bonds, being switched “ON” or “OFF.” Therefore,  $N_0$  is the sum of these ON and OFF bonds,  $N_0 = N_{\text{ON}} + N_{\text{OFF}}$ , with  $N_{\text{ON}}$  the work conjugate of the prescribed bond potential  $\Delta\mu$ . Analogous to insertion and deletion moves in GCMC-simulations, the ON and OFF setting of bonds is at the core of SGCMC trial moves, together with the bond topology of the considered texture model. The bond topology is dictated by the nearest neighbors of a mass point in the reference lattice. Randomly chosen ‘ON and OFF Monte Carlo moves are completed with alternating molecular dynamics (MD) runs in the  $NVT$  ensemble, to reach relaxed equilibrium states.

For purposes of illustration of the SGCMC simulation approach, we consider a face-centered cubic (FCC) lattice, with scale factor  $\sqrt{2}$ , for the reason of keeping identical the reference bond length,  $r_0 = 1$  in reduced units. The simulation box is a  $10 \times 10 \times 10$  lattice in a periodic box of side length  $L_0 = 10\sqrt{2}r_0$ , with four atoms in the unit cell for a total of 4000 atoms and 24 000 bonds (coordination number of the FCC lattice is 12).

Two types of bond potentials are considered: a truncated harmonic potential and a Morse potential, both defined by a ground-state energy parameter,  $\epsilon_i^0$ , and a stiffness parameter,  $k_i$ , in addition to the reference bond length,  $r_0$ , and cutoff distance for the harmonic potential,  $r_c = r_0(1 + \sqrt{2\epsilon_i^0/k_i})$ , so that, for the harmonic case,

$$U^H = \begin{cases} -\epsilon_i^0 + \frac{1}{2}k_i(r_i - r_0)^2, & r \leq r_c, \\ 0, & r > r_c. \end{cases} \quad (\text{A1})$$

And for the nonharmonic, Morse potential,

$$U_i^M = D_i(1 - \exp^{-\alpha(r_i - r_0)})^2 - D_i, \quad (\text{A2})$$

where the Morse parameters,  $D_i = \epsilon_i^0$  and  $\alpha_i = \sqrt{k_i/2D_i}$ , are obtained from a Taylor expansion of the Morse potential around  $r_0$ , in order to match the harmonic case. The approach can be extended to heterogeneous solids by considering a distribution of ground state energies and stiffness

values either through random placement or texture. Furthermore, reduced units are employed for the ground-state energy considering a low enough temperature (and associated thermal energy,  $k_B T$ ) for the FCC to be a solid; that is, in our simulations,  $T^* = k_B T / \epsilon_i^0 = 0.1$ . Similarly, due to the choice of the reference bond length,  $r_0 = 1$ , in reduced units, the stiffness parameter,  $k_i$ , is expressed in reduced units,  $k_i^* = k_i r_0^2 / \epsilon_i^0$ . The chosen value  $k_i^* = 61.32$  is representative of concrete when translating material properties into energy potential parameters in the lattice element method [44].

The SGCMC approach requires specifying the state variables of the SGC ensemble: bond rupture potential  $\Delta\mu$ , volume  $V$ , and temperature  $T$ , in addition to the constraint of a constant total bond number,  $N_0$ , fixed by the choice of the system (here,  $N_0 = 24\,000$ ). The prescribed volume is parametrized in the form  $V = V_0(1 + \epsilon_V)$ , with  $V_0$  the undeformed reference volume of the simulation box, and  $\epsilon_V$  the volume strain. In the quasistatic strain-controlled test, the volume is increased by equally stretching the simulation box side lengths  $L_x = L_y = L_z = L_0(1 + \lambda)$ . Strain increments of  $\lambda \approx \epsilon_V/3 = 0.1\%$  are prescribed followed by long enough MD simulations to reach quasistatic conditions in the displacement

controlled test. In these simulations, the reduced temperature is controlled by means of a Nosé-Hoover thermostat, with velocities sampled from a Gaussian distribution ensuring zero angular momentum. The time step in MD simulations is set to  $0.005\tau$  in Lennard-Jones reduced units (with unit LJ parameters). Between strain increments there are  $1,500\tau$  and  $2.1$  million SGCMC swap moves. As this is a Monte Carlo simulation, the time step is mostly relevant for the damping parameter of the Nose-Hoover thermostat, which is set to  $100\tau$ , in order to reach the prescribed temperature. Once relaxed, Monte Carlo simulations are carried out for each strain-controlled test (volume  $V_k$ ) at a given prescribed bond rupture potential,  $\Delta\mu_j$ , representative of the  $\Delta\mu_j V_k T$  ensemble. That is, to sweep the  $(\Delta\mu, V)$  phase space, a total of  $j \times k$  individual Monte Carlo simulations for each choice of prescribed energy functional (harmonic or Morse) are carried out. Starting with a fully bonded system,  $N = N_0$ , displacement loading is applied first before Monte Carlo simulations in the  $\Delta\mu_j V_k T$  ensemble are performed. These simulations are carried out with the LAMMPS Molecular Dynamics Simulator [45] and visualizations are created using the Open Visualization Tool (OVITO) [46].

- 
- [1] A. A. Griffith, *Philos. Trans. R. Soc. London A* **221**, 163 (1921).  
 [2] J. R. Rice, *J. Mech. Phys. Solids* **26**, 61 (1978).  
 [3] G. R. Irwin, *J. Appl. Mech.* **24**, 361 (1957).  
 [4] G. I. Barenblatt, *Adv. Appl. Mech.* **7**, 55 (1962). See also Willis's 1967 proof of the strict equivalence of the Fracture criteria of Griffith and Barenblatt in J. R. Willis, *J. Mech. Phys. Solids* **15**, 151 (1967).  
 [5] D. Dugdale, *J. Mech. Phys. Solids* **8**, 100 (1960).  
 [6] J. Hutchinson, *J. Mech. Phys. Solids* **16**, 13 (1968).  
 [7] Z. Yang, X. Su, J. Chen, and G. Liu, *Int. J. Solids Struct.* **46**, 3222 (2009).  
 [8] P. Ray, *Philos. Trans. R. Soc. London A* **377**, 20170396 (2018).  
 [9] H. J. Herrmann and S. Roux, *Statistical Models for the Fracture of Disordered Media* (Elsevier Science Publishers B. V., North-Holland, 1990).  
 [10] M. J. Alava, P. K. V. V. Nukala, and S. Zapperi, *Adv. Phys.* **55**, 349 (2006).  
 [11] J. Barés, M. L. Hattali, D. Dalmas, and D. Bonamy, *Phys. Rev. Lett.* **113**, 264301 (2014).  
 [12] E. Bouchaud, *Surf. Rev. Lett.* **10**, 797 (2003).  
 [13] S. Zapperi, P. Ray, H. E. Stanley, and A. Vespignani, *Phys. Rev. Lett.* **78**, 1408 (1997).  
 [14] J. R. Rice and R. Thomson, *Philos. Mag.* **29**, 73 (1974).  
 [15] B. de Celis, A. S. Argon, and S. Yip, *J. Appl. Phys.* **54**, 4864 (1983).  
 [16] K. Cheung and S. Yip, *Modell. Simul. Mater. Sci. Eng.* **2**, 865 (1994).  
 [17] J. Sinclair, *Philos. Mag.* **31**, 647 (1975).  
 [18] B. L. Holian and R. Ravelo, *Phys. Rev. B* **51**, 11275 (1995).  
 [19] M. Marder, *Int. J. Fract.* **130**, 517 (2004).  
 [20] M. J. Buehler, H. Gao, *Nature (London)* **439**, 307 (2006).  
 [21] H. Laubie, F. Radjai, R. Pellenq, and F.-J. Ulm, *J. Mech. Phys. Solids* **105**, 116 (2017).  
 [22] S. J. Zhou, P. S. Lomdahl, R. Thomson, and B. L. Holian, *Phys. Rev. Lett.* **76**, 2318 (1996).  
 [23] P. Gumbsch, S. J. Zhou, and B. L. Holian, *Phys. Rev. B* **55**, 3445 (1997).  
 [24] M. Marder and S. Gross, *J. Mech. Phys. Solids* **43**, 1 (1995).  
 [25] F. F. Abraham and J. Broughton, *Comput. Mater. Sci.* **10**, 1 (1998).  
 [26] J. Kermode, T. Albaret, D. Sherman, N. Bernstein, P. Gumbsch, M. Payne, G. Csanyi, and A. De Vita, *Nature (London)* **455**, 1224 (2008).  
 [27] E. Bouchbinder, J. Fineberg, and M. Marder, *Annu. Rev. Condens. Matter Phys.* **1**, 371 (2010).  
 [28] V. V. Ginzburg and L. I. Manevitch, *Int. J. Fract.* **64**, 93 (1993).  
 [29] R. Müller, E. Tadmor, R. Phillips, and M. Ortiz, *Modell. Simul. Mater. Sci. Eng.* **6**, 607 (1998).  
 [30] R. Perez and P. Gumbsch, *Phys. Rev. Lett.* **84**, 5347 (2000).  
 [31] B. R. Lawn, *J. Am. Ceram. Soc.* **66**, 83 (1983).  
 [32] J. Kermode, L. Ben-Bashat, F. Atrash, J. Silliers, D. Sherman, and A. De Vita, *Nat. Commun.* **4**, 2441 (2013).  
 [33] L. Brochard, G. Hantal, H. Laubie, F.-J. Ulm, R. J.-M. Pellenq, *Int. J. Fract.* **194**, 149 (2015).  
 [34] M. Bauchy, B. Wang, M. Wang, Y. Yu, M. J. A. Qomi, M. M. Smedskjaer, C. Bichara, F.-J. Ulm, and R. Pellenq, *Acta Mater.* **121**, 234 (2016).  
 [35] H. Laubie, F. Radjai, R. Pellenq, and F.-J. Ulm, *Phys. Rev. Lett.* **119**, 075501 (2017).  
 [36] D. Frenkel and B. Smit, *Understanding Molecular Simulation*, 2nd Edition (Academic Press, San Diego, 2001).  
 [37] P. M. Morse, *Phys. Rev.* **34**, 57 (1929).  
 [38] M. Camprostrini, A. Pelissetto, P. Rossi, and E. Vicari, *Phys. Rev. E* **65**, 066127 (2002).

- [39] M. Luban, *Phys. Rev. B* **7**, 2203 (1973).
- [40] See Supplemental Material at <http://link.aps.org/supplemental/10.1103/PhysRevE.103.013003> for a visualization of the potential energy evolution during the fracture process, as well as the formation of microcracks throughout the system converging into one macrocrack at failure.
- [41] D. Nicholson and N. G. Parsonage, *Computer Simulation and the Statistical Mechanics of Adsorption* (Academic, London, 1982).
- [42] R. J.-M. Pellenq and P. E. Levitz, *Mol. Phys.* **100**, 2059 (2002).
- [43] T. Al-Mulla, R. J.-M. Pellenq, and F.-J. Ulm, *Eng. Fract. Mech.* **199**, 544 (2018).
- [44] H. Laubie, S. Monfared, F. Radja, R. Pellenq, and F.-J. Ulm, *J. Nanomech. Micromech.* **7**, 4017007 (2017).
- [45] S. Plimpton, *J. Comput. Phys.* **117**, 1 (1995).
- [46] A. Stukowski, *Modell. Simul. Mater. Sci. Eng.* **18**, 015012 (2010).